

Nanoparticle Spectroscopy: Dipole Coupling in Two-Dimensional Arrays of L-Shaped Silver Nanoparticles

Jiha Sung, Erin M. Hicks, Richard P. Van Duyne, and Kenneth G. Spears*

Chemistry Department, Northwestern University, Evanston, Illinois 60208-3113

Received: March 19, 2007; In Final Form: May 10, 2007

The plasmon resonance was measured for two-dimensional arrays of L-shaped Ag nanoparticles fabricated by electron beam lithography. A variety of particle sizes were studied with nominal total edge lengths of ~ 150 nm, 63 nm arm widths, and 30 nm height. The single nanoparticle localized surface plasmon resonance (LSPR) of the L particles had two polarized components, which independently coupled in the arrays to create plasmon resonances for the array. The arrays had peak resonance locations and bandwidths that were dependent on grid spacing and particle number in the grid. The array plasmon resonance had a minimum bandwidth of $700\text{--}800\text{ cm}^{-1}$ at a grid spacing ~ 75 nm smaller than the grid having the largest red shift of the plasmon resonance. This bandwidth is about half the single nanoparticle resonance bandwidth. For arrays with small numbers of nanoparticles, the resonant wavelength and bandwidth had large deviations from the semi-infinite arrays but approached those results as the number of nanoparticles increased to 25 particles on an edge, which defines the range of effective dipole coupling for a 400 nm grid spacing. This observation is consistent with optical changes observed by scanning across a $300 \times 300\ \mu\text{m}^2$ pad. A solvent effect on these arrays demonstrated a red shift with similar bandwidth effects and some small grating-induced features due to waveguide effects.

I. Introduction

Nanomaterials are of current interest in a wide variety of fields from medicine to microelectronics. The optical properties of nanoscale-fabricated noble metal nanoparticles have drawn particular interest both experimentally and theoretically because of their impact in technological applications such as bio/chemosensors,^{1–4} optical filters,^{5,6} plasmonic waveguides,^{7–10} and substrates for surface-enhanced spectroscopies.^{11–13} The property behind all of these applications is the localized surface plasmon resonance (LSPR), which is a collective oscillation of the conduction electrons that occurs when light impinges on a nanoparticle at a specific wavelength. The resonance peak position and shape of the LSPR is governed by the nanoparticle shape, size, composition and dielectric environment. The LSPR resonance creates enhanced light scattering, absorption, and local enhancement of the electromagnetic field. For arrays of nanoparticles the LSPR optical properties become dependent on the array interactions to create a modified plasmon resonance that is characteristic of the whole array; therefore, one needs to understand nanoparticle coupling versus grid spacing, effects of shape and size, and the nanoparticle dielectric environment.

To effectively study a wide variety of arrays, a fabrication method is needed that has precise, user-defined placement of the nanoparticles. Current fabrication techniques include natural lithography, such as nanosphere lithography (NSL)^{14,15} and photolithography,^{16,17} and direct-write methods, such as electron beam lithography (EBL)^{18,19} or dip-pen nanolithography.²⁰ Each type has its own advantages and disadvantages, but for experiments involving the precise placement of nanoparticles on a surface, a direct-write method is an excellent tool. Specifically, EBL can be used to create nanoparticles with different shapes, sizes, spacing, and orientation in two-dimensional (2D) arrays.

A partial review of nanoparticle fabrication by EBL is given by Canfield et al.²¹

Optical properties of one- or two-dimensional noble metal nanoparticle arrays have been studied experimentally^{18,22–27} and theoretically by several groups. Short-range coupling effects in EBL fabricated hexagonal and square arrays of triangular and circular Au and Ag nanoparticles were studied optically by Van Duyne and co-workers.¹⁸ They observed a shift of the LSPR, depending on lattice spacing, and a related theoretical work explained these effects in terms of radiative dipolar coupling between the nanoparticles and retardation effects.^{18,28} For one-dimensional (1D) chains, they were able to experimentally find²⁵ a narrower shoulder on the plasmon resonance due to long-range dipole interactions along the chain, which was predicted by Schatz and co-workers.^{29,30} Others have looked in more detail at two-dimensional arrays with large grid spacing. Aussenegg and co-workers have studied extinction spectra of two-dimensional Au nanoparticle arrays with a variety of nanoparticle geometries such as cylinders,^{23,24,26} nanorods,^{23,24} and nanowire gratings.²⁷ In one study of Au arrays,²⁶ this group monitored the resonance peak with white light spectroscopy and the plasmon lifetime with time-resolved collinear autocorrelation measurements. They observed a red shift with increasing grid spacing and a dramatic increase in the plasmon damping at a critical grating constant. Their physical explanation for these effects relied on the models of Meier and Wokaun,^{31,32} and the experiments showed the importance of coherent scattering into a substrate as the means to enhance dipole coupling and thereby increase the radiative component of bandwidth. In a related recent work,²⁴ they showed a predicted grating-induced resonance^{31,32} in an array of Au nanorods having large transition dipoles. Others have looked into different shapes and lattice structures as well.^{32–34}

In this work we have studied an L-shaped nanoparticle, without a center of inversion symmetry, to provide optical characterization of linear optical properties prior to nonlinear optical studies of the same particles. For a nanoparticle or a lattice with in-plane center of inversion symmetry, the centrosymmetry of the in-plane dipole results in the cancellation of second-order nonlinear response such as second harmonic generation (SHG).^{35,36} Aussenneq and co-workers have studied the SHG response from a square lattice of Au nanoparticles created from three coalesced discs in a rough L shape. This work measured the plasmon dephasing time in the nanoparticles by interferometric autocorrelation methods.^{35,37} Tuovinen, Canfield, and co-workers^{21,38,39} studied the linear and second-order nonlinear optical properties of a two-dimensional array of L-shaped Au nanoparticles having rounded arms. They observed a polarization dependence in the linear and SHG response of L-shaped nanoparticle arrays. The extinction spectra were shown to have two optical transitions with independent polarizations along the mirror plane and perpendicular to the mirror plane. In their SHG studies, the incident laser wavelength was fixed at 1060 nm and they scanned the plasmon resonance of the array by changing the grid spacing.

There also have been efforts to theoretically predict and explain the modification of the optical properties of noble metal nanoparticles in 1D and 2D arrays. Wokaun and co-workers^{31,40} explained the resonant shift and bandwidth change of the plasmon of periodic nanoparticle arrays by dipolar interaction. With a coupled dipole model, Schatz and co-workers^{18,28} demonstrated that for the 1D and 2D periodic nanoparticle arrays the plasmon wavelength shift is determined by the real part of the retarded dipole sum, while the bandwidth is determined by the imaginary part of this sum. They also have shown that the bandwidth can reach a minimum for 2D arrays and that for 1D chains the polarization perpendicular to the chains gives exceptional opportunity for cancellation and extremely narrow bandwidths^{29,30,41} with uniform refractive index.

While the prior results give a conceptual basis for understanding some of the features of nanoparticle interactions in an array, more complete experimental data are required to provide data sets for more accurate testing of theoretical models and optimizing arrays for applications. A study with a fine set of grid spacings and comparison to isolated nanoparticles is presented here to explore how resonance positions and bandwidths depend on such parameters. In addition, we present the first study of different sized arrays having varying nanoparticle gaps in extended structures to show how resonances and bandwidths evolve with nanoparticle number and spacing. All of these studies are a prerequisite for understanding nonlinear optical properties of L-shaped particles and motivating new theory for linear and nonlinear optical properties of arrays. In this work we emphasize larger grid spacings and long-range dipole coupling effects.

In the following sections, we describe our optical studies of 2D arrays of Ag nanoparticles and the effects of grid spacing, environmental refractive index, and gaps within a 2D structure on the peak position and bandwidth of the plasmon resonance. Some discussion of theoretical models is used to rationalize our results, but more detailed theoretical modeling is in progress.

II. Experimental Section

A. Sample Fabrication. The samples were prepared by EBL on an indium–tin oxide (ITO) conducting layer of 40 nm on 750 μm thick glass substrates (Thin Film Devices, Anaheim, CA). The substrates were first cleaned by sonication for 5 min

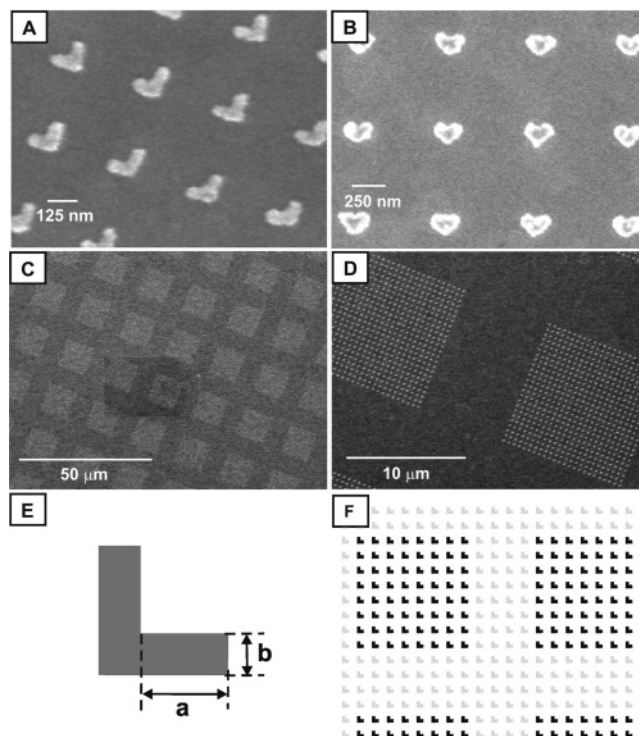


Figure 1. SEM images of two-dimensional arrays of L- and V-shaped nanoparticles. (A) L-shaped nanoparticle arrays (82 nm arm length, 250 nm grid spacing). (B) V-shaped nanoparticle arrays (83 nm arm length, 675 nm grid spacing). (C) Block-gap array of L particles with 82 nm arm length and 450 nm grid spacing (24 particles per block edge and gap of 17 particles). (D) Enlarged view of panel C. (E) Diagram of L-shaped nanoparticle. Dimension a is defined as the arm length and b is defined as arm thickness. (F) Diagram of gap arrays with 8×8 blocks and gap size of 4, where gray particles in the diagram stand for vacant sites.

in each of the following solvents: acetone, isopropyl alcohol, and DI water. The clean substrates were then baked at 170 $^{\circ}\text{C}$ for 1 min to remove any excess water from the surface. Each substrate was then spin-coated with a 70 nm film of an electron-sensitive resist, ZEP 520 (Nippon Zeon Ltd.) diluted 1:2 in anisole. Each sample was then soft-baked at 170 $^{\circ}\text{C}$ in a convection oven overnight. A Jeol 9300 FS was used to expose the resist; the resolution of the Jeol 9300 FS is approximately 6 nm, at an accelerating voltage of 100 kV. After exposure of the ZEP 520, the nanoparticle patterns were developed in hexyl acetate to create areas for deposition of Ag metal in a high-vacuum thin-film vapor deposition system (AVAC HVC 600). For all samples the metal thickness is 30 nm, as measured by a quartz crystal microbalance. In the last step of the sample preparation, the lift-off step, the resist was dissolved in a strong solvent (Shipley remover 1165), which also removes the metal deposited on top of the resist. To ensure that the metal film on top of the resist does not have any physical contact with the metal deposited directly on the substrate, samples were prepared with an “undercut” in the resist film. This is accomplished by overdeveloping the resist slightly. In this work, nanoparticles shaped like an L, with equal arms, were used in two orientations, which we call L or V depending on their orientation relative to lines of nanoparticles (see Figure 1). We studied both continuous arrays over large areas of $\sim 100 \times 100 \mu\text{m}^2$ and arrays with gaps. Gap arrays are those where different unit cells were repeated with “missing” nanoparticles or gaps; this gives translational symmetry to the whole array. Scanning electron microscopic (SEM) images to clarify this structure can be seen in Figure 1. For the L structure we use arm length to refer to

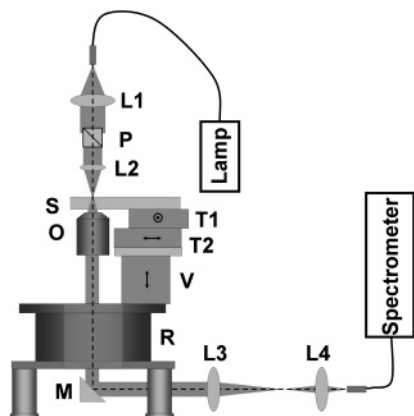


Figure 2. Experimental setup used for extinction measurements. Symbols represent achromatic lenses (L1–L4), polarizer (P), sample mount or flow cell (S), 10× Nikon microscope objective (O), computer-controlled microtranslational stages (T1 and T2), vertical stage (V), rotational stage (R), and a mirror (M). The focal lengths of achromatic lenses are +40 mm, +12.7 mm, +200 mm, and +30 mm, respectively. The microscope objective is attached to its own manual *xyz*-translational stage, which is not shown in this figure.

the extension past the thickness of the arm, which is 63 ± 5 nm; for example, an 82 ± 5 nm arm length has a full edge length of 145 nm in both directions. Figure 1E shows the definition of arm length and arm width of L-shaped nanoparticle. Tables 1 and 2 summarize all the arrays reported in this paper. In each sample we prepared duplicate and triplicate arrays, and in the following plots data for two or three duplicate samples are shown. These duplicates show reproducibility of the EBL method. EBL fabrication was performed at the MC2 process lab at Chalmers University of Technology.

B. White Light Spectroscopy. Extinction spectra were collected on an Ocean Optics USB2000 fiber-coupled spectrometer for the 400–1000 nm region and a fiber-coupled near-infrared (NIR) spectrometer (NIR 128L-1.7T1-USB, Control Development) for the 900–1700 nm region. The Ocean Optics had low noise to 950 nm. The spectra over this wide region have a slight mismatch near 900 nm, signifying where one spectrometer ends and the other begins. The optics arrangement is shown schematically in Figure 2. White light from a tungsten-halogen lamp light source was fiber-coupled with a 100 μm fiber to a +40 mm focal length achromatic collimating lens. The collimated beam was then polarized by a Glan-Taylor calcite polarizer with 5 mm aperture and focused onto the sample by a +12.7 mm focal length achromatic lens with the optic axis normal to the sample surface. Transmitted light was collected by an infinity-corrected 10× Nikon microscope objective (NA = 0.30) at a working distance of 16.0 mm and focused into a 600 μm fiber that couples into the spectrometer. The white light spot size on the sample was scanned with a straight edge and was close to Gaussian with a 20 μm diameter at full width at half-maximum (fwhm).

The sample was mounted on two computer-controlled microtranslational stages (M-111.1DG, Physik Instrumente) to

form an *x*–*y* system with a 50 nm step size. The *x*–*y* stage system is fixed on the manual vertical linear stage (MVN50, Newport Corp.) and manual rotational stage (M-UTR120A, Newport Corp.). Rotation of the incident beam polarization relative to the sample geometry was achieved by rotating the sample stage with fixed incident beam polarization. The white light axis is coincident with the rotational axis of a rotational stage to make the beam position fixed on the sample during sample rotation. All the samples were studied under a stream of dry nitrogen, with some additional samples being tested in benzene as well. The extinction measurement was done approximately at the center of the $\sim 100 \times 100 \mu\text{m}^2$ pads, and the reference measurement was obtained by scanning into a nearby region of the glass substrate.

C. Dark-Field Scattering Measurement. A single nanoparticle scattering spectrum of the high-energy band was obtained by resonant Rayleigh dark-field optical microscopy with an inverted microscope (Eclipse TE300, Nikon Instruments) equipped with a dark-field condenser (NA = 0.95–0.80) for illumination and a 40× objective (NA = 0.60) for collection. White light from the tungsten-halogen lamp in the microscope was polarized by a linear polarizer (cutoff ~ 800 nm) before the dark-field condenser. The dark-field condenser system was modified to improve transmitted polarization by a mask having a wide slit along a radius aligned with the input polarization. The transmitted polarization still shows a weak component from orthogonal polarized transitions. Collected light was directed to an imaging spectrograph (SpectraPro 300i, Roper Scientific) coupled with a liquid nitrogen-cooled charge-coupled device (CCD) camera (Spec-10:400B, Roper Scientific).

D. Structural Characterization of Nanoparticle Arrays. The EBL patterns were characterized with scanning electron microscopy. Accelerating voltages used for imaging were 5–10 kV with a working distance of 7 mm. In Figure 1, images of different shapes and arrangements are shown. Imaging was performed in the EPIC center at Northwestern University with a Hitachi 4500.

III. Results

A. Structural Characterization. The shape of nanoparticles in 2D L-shaped nanoparticle arrays (L arrays) is sharper than that of 2D V-shaped nanoparticle arrays (V arrays), and these variations are according to each particular run of the EBL machine (see Figure 1). Grid spacing is varied from 250 to 650 nm for L arrays and from 400 to 750 nm for V arrays. A 2D array with 5 μm grid spacing is also fabricated to provide spectra of “isolated” nanoparticles due to negligible dipole interactions at this spacing. For most studies, sample pads with $100 \times 100 \mu\text{m}^2$ dimension were fabricated, and a $300 \times 300 \mu\text{m}^2$ pad was fabricated to explore edge effects from the dipole coupling (see section C following). Gap arrays of smaller size were created by isolating smaller blocks with gaps within the same $100 \times 100 \mu\text{m}^2$ pad. These were fabricated to study the range of dipole coupling in finite arrays; our samples maintain translational

TABLE 1: Characteristics of 2D Ag Nanoparticle Square Arrays

orientation	arm length ^a (nm)	arm width ^a (nm)	grid spacing (nm)
L	82	63	250, 300, 350, 400, 420, 440, 450, 460, 500, 550, 600, 650, 5000
L	92	63	250, 300, 350, 400, 420, 440, 450, 460, 500, 550, 600, 650, 5000
V	83	93	400, 450, 475, 500, 525, 550, 575, 600, 625, 650, 675, 700, 725, 750, 5000
V	103	93	400, 450, 475, 500, 525, 550, 575, 600, 625, 650, 675, 700, 725, 750, 5000

^a Error is ± 5 nm.

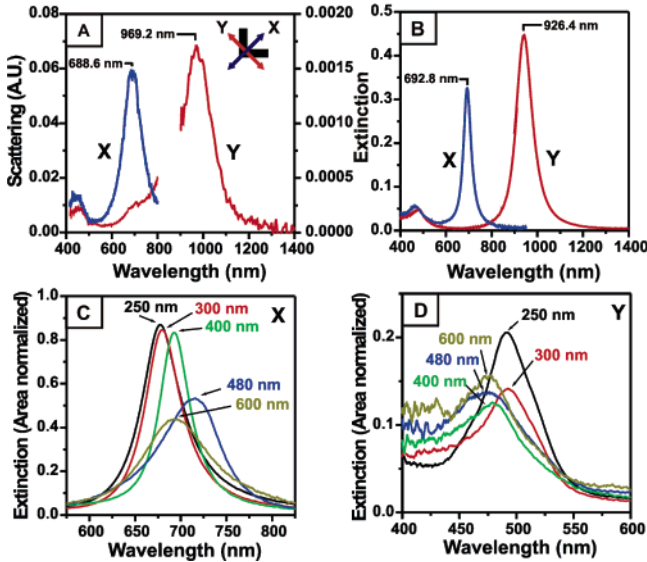


Figure 3. (A) Dark-field scattering spectrum (400–800 nm) of a single, 82 nm arm length, L-shaped nanoparticle (X band) from a 5 μm grid spacing array and extinction spectrum (>900 nm, Y band) of this array. Inset shows a definition of the incident beam polarizations used for these experiments. (B) Extinction spectra of 2D array of 82 nm arm length L-shaped nanoparticles with 400 nm grid spacing. (C) Spectra of the X-polarized dipole band for selected grid spacing; 250 nm (black), 300 nm (red), 400 nm (green), 480 nm (blue), and 600 nm (dark yellow). (D) Spectra of the nonpolarized band with a Y-polarized incident beam for selected grid spacings.

symmetry for fixed grid spacing and nanoparticle parameters with variable gaps and variable numbers of nanoparticles in each block.

B. Plasmon Resonance Position and Bandwidth in Isolated Nanoparticle and 2D Arrays. The polarization-dependent spectra of isolated L-shaped nanoparticles and a 400 nm spaced square array of L-shaped nanoparticles are shown in Figure 3A,B. Two independent bands can be observed in the isolated nanoparticle spectra (Figure 3A) with orthogonal incident beam polarization. The high-energy band in these spectra was studied with a dark-field scattering method on a single nanoparticle in a pad with 5 μm grid spacing, and the low-energy band was obtained by extinction measurement on a pad with 5 μm grid spacing. These two transitions are maintained in the 2D arrays (Figure 3B). The inset in Figure 3A is a definition of the polarizations used for these experiments. For both 2D L and 2D V arrays, as well as for isolated nanoparticles, when the polarization is along the mirror symmetry plane of the nanoparticle (X polarization), a high-energy band is observed, and when the polarization is perpendicular to the symmetry plane (Y polarization), a low-energy band is observed. When the polarization is in between, both bands are observed. However, the resonant wavelength and bandwidth of the isolated nanoparticles are different from those of the 2D array, and the resonant wavelength and bandwidth of the 2D array also changes for other grid spacings. In Figure 3C we see that at 400 nm grid spacing the spectrum shows the narrowest bandwidth, and

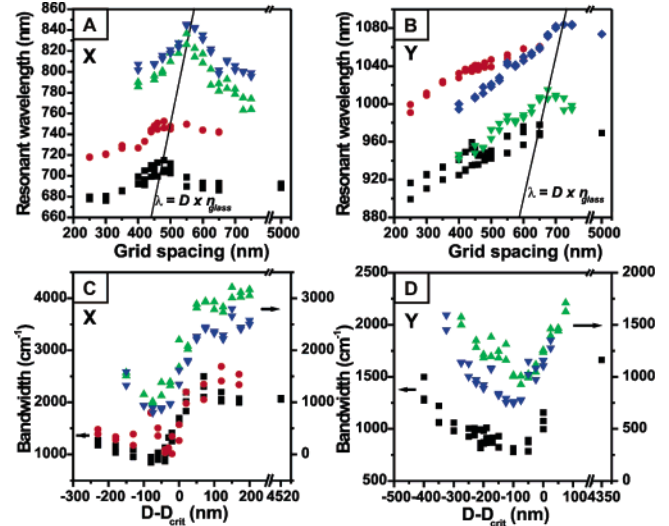


Figure 4. Resonant wavelength and bandwidth versus grid spacing for X-polarized extinction (A, C) and Y-polarized extinction (B, D) for 2D nanoparticle arrays of L and V orientation. L arrays with 82 and 92 nm arm length are plotted with black squares and red circles, respectively, and V arrays with 83 and 103 nm arm length are plotted with green triangles and blue inverted triangles, respectively. Duplicate and triplicate (82 nm L, black) arrays are shown for different array pads prepared on the same chip. The line $\lambda = D \times n_{\text{glass}}$ is shown with a black solid line in panels A and B. The bandwidth is plotted versus $(D - D_{\text{crit}})$, where D is the actual grid spacing and D_{crit} is the critical grid spacing where the resonant wavelength shows maximum red shift. Plots for L arrays follow the left axis, and the plots for V arrays follow the right axis.

at 480 nm grid spacing the resonant wavelength of the spectrum shows the most red shift. Note that the spectrum at 480 nm grid spacing is quite distorted from a Lorentzian line shape.

In Figure 3A,B, there is a weak band at ~ 450 nm; it does not change by rotation of the incident beam polarization and is not very dependent on grid spacing. These features suggest that this band might be a more complex resonance, and we will refer to it as the nonpolarized extinction band. Figure 3D shows the nonpolarized band of the 2D L arrays with Y-polarized incident beam. A similar spectrum is observed for the X-polarized incident beam, which is not shown. At more closely spaced grids of 250 and 300 nm, the amplitude of this band increases with a slight red shift, and this effect is shown for all 2D L arrays with different arm lengths.

We systematically prepared samples to study the grid spacing effect, and the results are shown in Figure 4A,B. Two data points are often visible for duplicate arrays made in the same preparation, although most are overlapping. The isolated particle parameters are obtained from the data with 5 μm grid spacing. We see that as the grid spacing changes, the resonant wavelength of the absorption changes for both array types. The resonant wavelength red-shifts with increasing grid spacing and reaches a maximum red shift at a critical grid spacing (D_{crit}). At larger grid spacing the resonance wavelength begins to blue-shift. The value of D_{crit} is indicated in the figures at the grid spacing where

TABLE 2: Characteristics of Ag Nanoparticle Gap Arrays

orientation	arm length ^a (nm)	arm width ^a (nm)	grid spacing (nm)	block size ^b	gap size ^b
L	82	63	450	24 \times 24	17
L	92	63	400	8 \times 8	4, 9, 17
L	92	63	400	12 \times 12	4, 9, 17
L	92	63	400	16 \times 16	9, 17
L	92	63	400	24 \times 24	9, 17, 25

^a Error is ± 5 nm. ^b Numbers of particles.

the resonant wavelength is coincident with Dn_{glass} where D is grid spacing and n_{glass} is the refractive index of glass ($n_{\text{glass}} = 1.5$). Not only the peak position but also the bandwidth changes as the grid spacing is changed. Figure 4C,D depicts the plots of the resonance bandwidth versus $(D - D_{\text{crit}})$. For both high-energy (X-polarized) and low-energy (Y-polarized) dipole bands, the bandwidth decreases as the grid spacing increases until a particular spacing, where it starts increasing as spacing increases. This bandwidth turnover occurs at a spacing that is about 75 nm smaller than the D_{crit} of each band. The minimum bandwidth achieved with an optimized 2D array is about half the single nanoparticle resonance.

The resonance band shape of most grid spacings is a Lorentzian function except when the grid spacing is near D_{crit} . The spacings with Lorentzian line shapes indicate that there is no large inhomogeneous broadening in these nanoparticles. When the grid spacing is close to D_{crit} , the line shape of resonance band starts deviating from the Lorentzian, and this distortion lasts until ~ 100 nm larger spacing than D_{crit} . When the grid spacing is just larger than the turnover of bandwidth, the band shape becomes distorted significantly and forms a broad shoulder on the high-energy side, as can be seen in the 480 nm grid of Figure 3C. In case of bands with Lorentzian shape, the product of lifetime in time domain and bandwidth in frequency domain is $1/2\pi$. The minimum bandwidth observed was around $700\text{--}800\text{ cm}^{-1}$ (~ 0.1 eV), and it corresponds to a plasmon lifetimes of $7.6\text{--}6.6$ fs.

C. Range of Dipole Coupling. To explore the plasmonic coupling in these arrays, $100 \times 100\ \mu\text{m}^2$ gap arrays were fabricated with different unit sizes and gap sizes between the units (each unit is a smaller square block of nanoparticles, and in our discussion we refer to these as blocks). The pattern is shown in Figure 1C,D for a specific case, and in Figure 1F we show a detailed diagram of gap arrays with 8×8 blocks and gap size of 4. Gray particles in Figure 1F stand for vacant sites. All the gap-arrays tested have L orientation and are summarized in Table 2. The resonant wavelength of each gap array is shown in Figure 5A,B for each high- and low-energy band. For the smallest block size, an 8×8 nanoparticle block, high- and low-energy bands are red-shifted from that of semi-infinite array. The magnitude of the shift is different for each band, with a shift of ~ 50 nm for the low-energy band and ~ 10 nm for the high-energy band. As the number of nanoparticles in a block is systematically increased from 8×8 to 24×24 , the plasmon peak position blue-shifts and approximately converges to the peak position of a semi-infinite nanoparticle array.

The resonance bandwidth also shows a large change according to the block dimension. Figure 5C,D show a plot of the bandwidth versus block dimension. As the block size increases, the bandwidth decreases and it converges to that of semi-infinite nanoparticle array. However, the gap dimension does not seem to play a significant role in either the resonant wavelength or the bandwidth. There is no systematic trend in resonant wavelength and bandwidth according to the change of gap dimension. Furthermore, for some nanoparticle blocks, such as 16×16 blocks, different gaps show almost the same resonant wavelength and bandwidth; this suggests that four or more nanoparticle gaps isolate the unit blocks. These results are shown for a grid spacing of 400 nm; a similar set of results was found for a spacing of 450 nm, which is not shown.

To explore the consistency of the resonant wavelength and the bandwidth of the LSPR across a nanoparticle array, large arrays ($300 \times 300\ \mu\text{m}^2$; grid spacing = 250 nm) were fabricated and spectra were taken at various positions throughout the array.

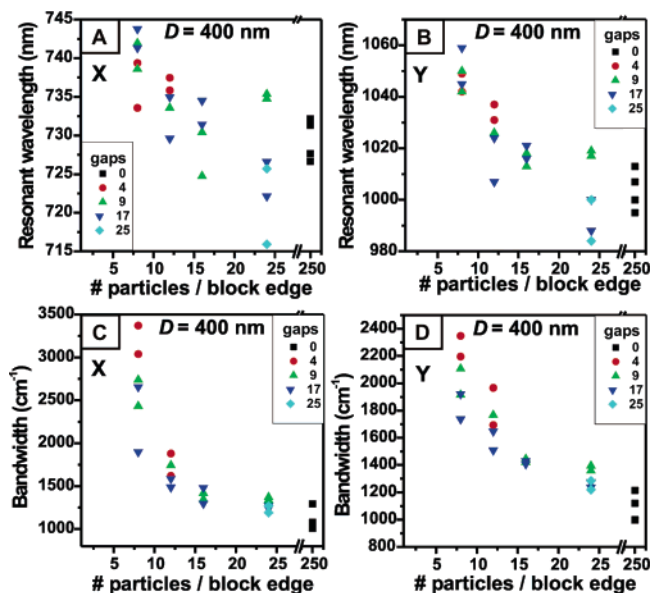


Figure 5. Resonant wavelength and bandwidth of X-polarized bands (A, C) and Y-polarized bands (B, D) of gap-array samples (L arrays, 92 nm arm length, 400 nm grid) versus the number of particles per block edge. Data for semi-infinite particle arrays are plotted with black squares, and data with gaps corresponding to 4, 9, 17, and 25 particles are plotted with red circles, green triangles, blue inverted triangles, and cyan diamonds, respectively. Duplicate arrays are shown for different array pads prepared on the same chip.

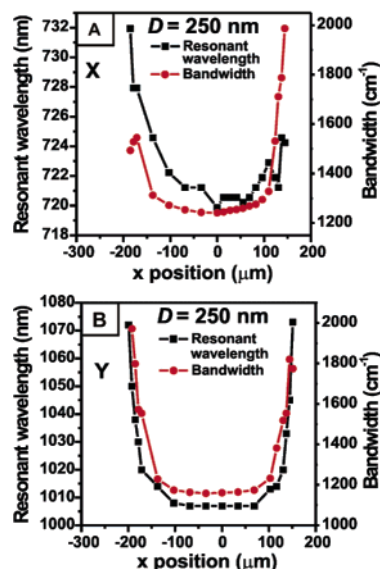


Figure 6. Resonant wavelength and bandwidth of X-polarized band (A) and Y-polarized band (B) scanned from one edge to the other edge of the two-dimensional L-shaped nanoparticle array. The array dimension was $300 \times 300\ \mu\text{m}^2$. The arm length of the particle was 92 nm, the grid spacing was 250 nm, and the focal spot radius for 99% of the energy was $\sim 19\ \mu\text{m}$.

These results are in Figure 6 where one observes that as the probe beam gets closer to the edge of the pad, the peak position red-shifts and the bandwidth becomes broader. The origin ($x, y = 0$) is arbitrarily set in both directions, and the data were not rescaled to be symmetric.

D. Solvent Effect on Plasmon Resonance of 2D Arrays. As stated in the beginning of the paper, the LSPR resonance position is a function of many parameters, including the refractive index of the medium surrounding the nanoparticles. The Mie theory for spherical nanoparticles⁴² and the experiments

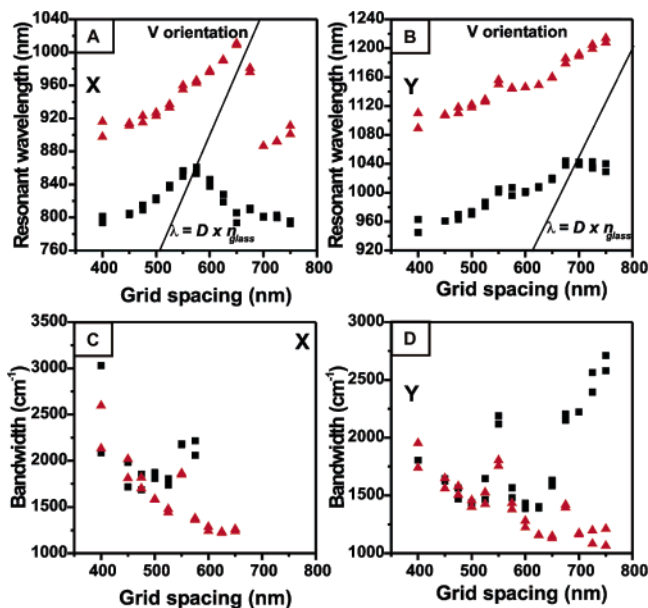


Figure 7. Resonant wavelength and bandwidth of the X-polarized band (A, C) and Y-polarized band (B, D) in two different dielectric media: nitrogen ($n = 1.0$) and benzene ($n = 1.5$). The sample was 2D V arrays with 83 nm arm length. Duplicate arrays are shown for different array pads prepared on the same chip. The plot with black squares is in nitrogen, and the plot with red triangles is in benzene. The line $\lambda = Dn_{\text{glass}}$ is shown with a black solid line.

and theoretical calculations of various types of nanoparticles^{15,43–45} describe the plasmon shift in dielectric media other than vacuum.

The two dipole bands of V arrays with 83 nm arm length were monitored in nitrogen and benzene. The change in resonance wavelength and bandwidth for different grid spacing in nitrogen and benzene is shown in Figure 7. Figure 7A,B shows the resonant wavelength versus grid spacing plots for both high- and low-energy bands in two different dielectric media for the same sample. In benzene ($n = 1.5$), the resonant wavelength shifted to the red compared to nitrogen ($n = 1.0$), as expected from the increase in refractive index. D_{crit} of the high-energy band shifted from ~575 nm in nitrogen to ~650 nm in benzene. D_{crit} of the low-energy band is ~700 nm in nitrogen; however, in benzene, it is not observed within our grid spacing range.

Figure 7C,D shows the bandwidth versus grid spacing plot for both high- and low-energy bands. In the high-energy band (Figure 7C) we see that the nitrogen case has a minimum in bandwidth at about 525 nm grid spacing, or 50 nm below the D_{crit} . However, the case of benzene shows no clear minimum in bandwidth until about 625 nm, which is slightly below its D_{crit} . In the low-energy band (Figure 7D), the bandwidth of the LSPR band in two different environments is similar to each other at grids smaller than 600 nm. However, in nitrogen it starts increasing after this spacing, while in benzene it keeps decreasing because D_{crit} is moved to larger grid spacing.

An alternative way to examine the data is to plot the difference between the high- and low-energy resonances in nitrogen and benzene. In Figure 8 we see the energy difference between the high- and low-energy bands in nitrogen is the same up to the point of D_{crit} in the nitrogen data at 575 nm (see Figure 7A).

When benzene is introduced as a dielectric medium, an additional band was observed that was not seen under nitrogen (Figure 9A,B). This feature shifts to red as the grid spacing increases, and it is assigned as grating-induced plasmon mode as seen previously by Félidj et al.²⁴ This mode was not observed

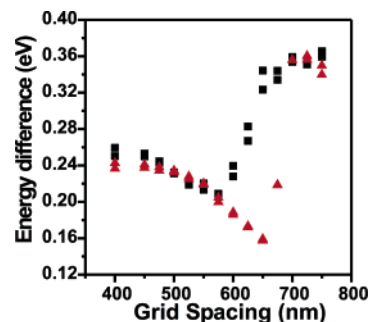


Figure 8. Energy difference between X- and Y-polarized bands in nitrogen (black square plot) and in benzene (red triangle plot). Duplicate arrays are shown for different array pads prepared on the same chip.

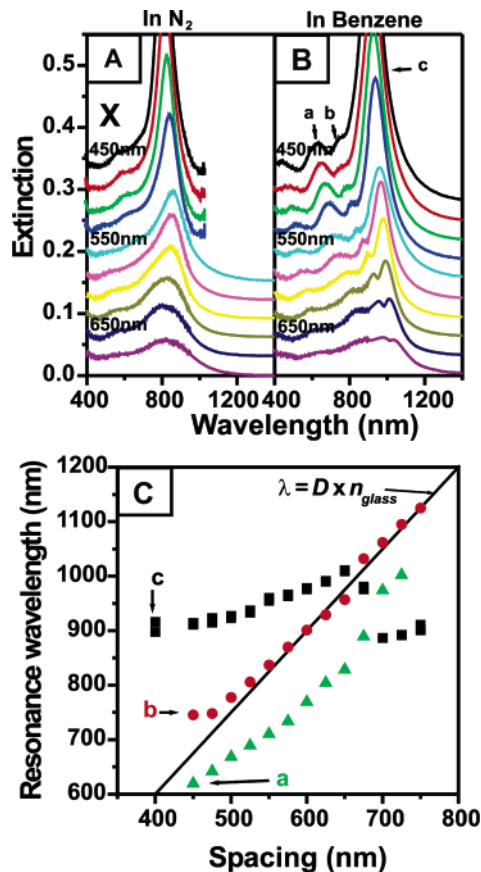


Figure 9. (A) Extinction spectra of the 2D V arrays with different grid spacings in nitrogen. Grid spacing ranges from 450 to 675 nm in 25 nm increments from top to bottom. All the spectra are shown with an offset for clarity. The arm length of the V nanoparticle was 83 nm. (B) Extinction spectra of the 2D V arrays in benzene. Grid spacing is the same as in panel A. (C) Resonant wavelength of X-polarized band, marked as c in panel B, is plotted with black squares (duplicate arrays are shown for different array pads prepared on the same chip), and grating-induced plasmon mode, marked as b in panel B, is plotted with red circles. The grating-induced mode follows $\lambda = Dn_{\text{glass}}$ line. Another resonance, marked as a in panel B, is plotted with green triangles.

under nitrogen because 40 nm ITO cannot support as a waveguide with a low index on one side.^{46,47} When the refractive index of the medium on top of the 40 nm ITO layer is close to 1, that is, the refractive index of nitrogen, the cutoff frequency for waveguide operation is located in the UV range. However, as the refractive index of the medium approaches that of glass substrate, the cutoff frequency moves to low frequency. Therefore, in benzene, the ITO waveguide mode can support visible and near-IR wavelengths, and this creates the additional feature in the extinction spectrum. In Figure 9C, the grating-

induced plasmon mode is plotted with red circles while the high-energy band resonance is plotted with black squares. The grating-induced mode follows the $\lambda = Dn_{\text{glass}}$ line, and this agrees with the observation reported by F elidj et al.²⁴ It is also observed for a low-energy mode, which is not shown here.

IV. Discussion

Resonances having polarization properties similar to those shown in Figure 3 have been reported for arrays of Au nanoparticles of a rounded L shape^{21,38,39,48} but not for isolated nanoparticles. Our fabrication procedure often resulted in less rounded arms for individual L nanoparticles, and these Ag nanoparticles have two main polarized transitions, with a small nonpolarized transition to the blue of the main transitions. The position of the nonpolarized transition is not sensitive to grid spacing, but it increases its amplitude at close spacings of 250 and 300 nm and it also exists in the isolated nanoparticle. Preliminary theoretical results confirm that a small nonpolarized extinction is expected to the blue of the two polarized resonances.

The shifts in location of the polarized resonances as a function of grid spacing have been seen previously for close-spaced grids¹⁸ and for grids having similar spacing ranges to this work.²⁶ Figure 4 shows a variety of L sizes and two orientations for both the blue and red resonances of our nanoparticles. The results in Figure 4A,B show the same grid spacing dependence as was seen previously,²⁶ with a resonance peak position shifting red as the grid spacing increases. This shift reverses at some critical grid spacing D_{crit} , and then returns to a value similar to the isolated nanoparticle resonance at larger spacing. We expect the limiting value at very large spacing to be identical to the average isolated nanoparticle resonance. The maximum resonance shift has been discussed previously²⁶ as being defined by the wavelength where scattering can propagate in the substrate with grazing angle, which for our normal incidence geometry is at the glass index (~ 1.5) of refraction (n_{glass}) times the grid spacing (D). In prior theoretical work^{31,32} this type of shifting was predicted as due to dipole interactions with enhancement from scattering into the substrate. This model provides a qualitative understanding of why the bandwidth is also changing dramatically,²⁶ as shown in Figure 4C,D. The physical interpretation of this model shows that the greatest bandwidth should be at a grid where maximum radiation into the substrate is present, which enhances radiation damping and shortens the lifetime below the intrinsic electron–hole relaxation time. When the grid spacing is small compared to the wavelength of the plasmon resonance, radiative damping and intrinsic relaxation define the line width. As the grid spacing times the glass refractive index (Dn_{glass}) approaches the plasmon resonance wavelength, maximum dipole interactions between particles shift the peak resonance due to coherent interactions. These interactions near the wavelength Dn_{glass} provide increased radiative damping, which broadens the Lorentzian line shape. All of the samples give the narrowest bandwidth at a similar value of ~ 75 nm for $(D - D_{\text{crit}})$. However, specific computation is required to predict how narrow the minimum bandwidth might become and the origin of the 75 nm offset for minimum bandwidth.

Another type of model has identified how the dipole coupling explains red or blue shifts in the resonances.^{18,28} A simple semianalytical model of coupled dipoles²⁸ shows how summing all of the dipole interactions on an infinite lattice can be modeled with optical constants of the metal and computation of the extinction. While this study did not extend to larger grid spacing, they showed that the bandwidth is controlled by the imaginary

part of the sum of all dipole contributions and the resonance is controlled by the real component. Red shifting was shown to be expected for grid spacing similar to the isolated nanoparticle resonance and blue shifts for closer spacing. By analyzing the polarization of the whole array in this fashion, they show that long-range dipole contributions dominate for 2D lattices. The simplified model was also used to examine 2D array data at relatively close spacings.¹⁸ The resonance shifts are qualitatively consistent with the data; however, the simplified model was not extended to large grid spacings. One electrodynamic calculation was done for 400 spherical Ag nanoparticles of 50 nm diameter on 2D grids.^{29,30} This calculation shows a progressive narrowing of the resonance with increasing grid spacing, along with the red shift. The grid spacing of minimum bandwidth is 500 nm, with a bandwidth of 0.084 eV, which is similar to our narrowest bandwidth. However, the line shape for resonances is different from our experiments. In the theoretical work, as the grid becomes larger the line shapes look like an interference dip plus a red resonance adding to the broad resonance of an isolated nanoparticle. We have used the simplified coupled dipole model²⁸ to show that this general form is also present at larger grid spacings with no substrate; we find the interference dip for ellipses at the wavelength of the grid spacing. Therefore, the experimental line shapes do not agree with the theoretical line shape that has been predicted for arrays of spherical nanoparticles,^{29,30} although the minimum bandwidth is close to our data. However, our experiments with an ITO glass interface do not follow the theoretical conditions of uniform refractive index, even in benzene solution. Our work and the prior work on Au nanoparticles find a Lorentzian line shape for most wavelengths, except when the grid is near the grid of maximum red shift D_{crit} . Additional theoretical work on nonspherical particles that includes substrate effects is required to model these changes in line shape as a function of grid spacing and the location of the minimum bandwidth point.

The data on gap arrays relate to the basic interpretation of dipole interaction discussed in the prior paragraph. Figure 5A,B shows how the resonance position shifts as the number of nanoparticles in the 2D arrays increases. The resonance position data show significant fluctuation so that any dependence of the trend on gap size is not obvious. However, the size of the array clearly correlates with the resonance position, with larger numbers of nanoparticles having a resonance that approaches the limiting large array value. Figure 5C,D shows that the number of nanoparticles greatly affects the bandwidth. Here we see a dramatic reduction in bandwidth as the number of nanoparticles increases. For the smaller gap arrays of 8×8 and 12×12 nanoparticles, the data suggest that gaps of four nanoparticles have greater bandwidth than larger gaps, but this might be due to sample variations, and more study with even smaller gaps is in progress. The greater bandwidth of smaller arrays is clear from these data, and it suggests that 24×24 nanoparticles is approaching the number of dipole interactions required to give similar effects to a full array. For this particular grid spacing of 400 nm, the full array has a bandwidth near the minimum value, which is achieved at 450 nm grid spacing. The dependence of bandwidth on nanoparticle number suggests that the minimum bandwidth is a consequence of many dipole interactions reducing the natural radiative scattering probability. Additional theory is required to explain the nanoparticle number dependence of the bandwidth and define the ultimate minimum bandwidth. The range of nanoparticle interaction in these experiments exceeds 25 nanoparticles with 400 nm spacing, or 10 μm . While not tested, one might expect the coupled

nanoparticle range of 40 nanoparticles might closely approach the infinite limit, or 16 μm .

Figure 6 shows how the range of dipole interactions depends on the experimental setup. For an optical focus of 20 μm fwhm, which is smaller than the array size of $300 \times 300 \mu\text{m}^2$, we can clearly see the effects of approaching an edge. In Figure 6B we find about 200–220 μm out of the 300 μm size to have the limiting bandwidth. The beam focus radius to the 99% energy level is 18.7 μm , although the sharpness of the focus in this particular experiment was not immediately measured and might be slightly different. If we use this radius and a nanoparticle interaction range of 16 μm to define a reasonable approximation to an infinite lattice, then the sum of these effects is about 35 μm . This would predict a constant range of 230 μm in the data for Figure 6B, which is slightly larger than we measured. This shows that optical scanning of arrays requires careful attention to edge effects in the probe beam and the range of dipole interactions and is important for designing sensing applications.

The solvent experiments shown in Figure 7 have the effect of approximately immersing the nanoparticles into a constant refractive index environment. The red shifts of resonances were similar to other types of nanoparticle arrays,^{15,45} and the bandwidth changes in benzene are similar to data in nitrogen. Figure 8 shows that the splitting between the resonances is almost constant up to D_{crit} . These results show that the minimum bandwidth effects can be maintained in solvents, which might be important for sensing applications. The effect of a constant refractive index environment at enhancing waveguide effects was shown in Figure 9. For a study of nanoparticle effects in solution it would be better to not use ITO, although it makes the fabrication easier.

V. Conclusion

The LSPR extinction spectra of 2D arrays of Ag nanoparticles having an L shape were obtained for various grid spacings and nanoparticle sizes. Single nanoparticles had two independent extinction resonances with orthogonal polarization, and the two resonances were maintained in the 2D arrays. A small resonance to the blue of the main resonances was not polarized, and it suggests a more complex optical transition that had changes in amplitude and resonance at close grid spacing of 250 and 300 nm. Each polarized resonance had its resonance wavelength and bandwidth modified by the grid spacing of 2D arrays. The maximum resonance red shift was shown at a critical grid spacing, D_{crit} , defined previously²⁶ as the spacing where scattering launches into the substrate. The minimum bandwidth was observed at ~ 75 nm smaller grid spacing than the critical grid spacing for each high- and low-energy band. The minimum bandwidth of 700–800 cm^{-1} is half the single nanoparticle resonance and corresponds to 7.6–6.6 fs lifetime. The number of interacting nanoparticles also determined the resonant wavelength and bandwidth, with bandwidth most sensitive. As the number of interacting nanoparticles increased from an 8×8 to a 24×24 array, the resonant wavelength red-shifted and bandwidth decreased to near the semi-infinite array limit. However changing the gap between adjacent 2D blocks from 4 to 25 nanoparticles did not play a discernible role in resonant wavelength and bandwidth, although fabrication issues create noise in the data. More experiments are needed with gaps from 1 to 4 particles. The effect of dipole coupling range was also shown by scanning a larger array, where edge effects in resonance position and bandwidth could be clearly shown. When the refractive index of the environment was increased by adding solvent, the resonant wavelength shifted to the red. The critical

grid spacing and the spacing for minimum bandwidth shifted accordingly. This solvent effect shows that specific grid spacing can achieve minimum bandwidth, which is important for sensing applications in solvents. The energy difference between the high- and low-energy band was approximately constant in nitrogen and benzene. The refractive index similarity of benzene to a glass substrate enables a waveguide mode to be supported by a 40 nm ITO layer. Therefore, in benzene a small grating-induced resonance was observed, which was not observed in a nitrogen environment.

Acknowledgment. We gratefully acknowledge support from the Air Force Office of Scientific Research (MURI Program Grant F49620-02-1-0381). Additionally, R.P.V.D. acknowledges support from the National Science Foundation (CHE-0414554, DMR-0520513). We thank Dr. George C. Schatz, Dr. Linlin Zhao, Dr. Maxim Sukharev, and Dr. Tamar Seideman for helpful discussions and preliminary modeling of L particles. We acknowledge the MC2 process lab at Chalmers University of Technology for access to their facilities. We also acknowledge the Käll group for their help and guidance while the work was performed at MC2.

References and Notes

- (1) Haes, A. J.; Van Duyne, R. P. *J. Am. Chem. Soc.* **2002**, *124*, 10596.
- (2) Haes, A. J.; Chang, L.; Klein, W. L.; Van Duyne, R. P. *J. Am. Chem. Soc.* **2005**, *127*, 2264.
- (3) Henglein, A.; Meisel, D. *J. Phys. Chem. B* **1998**, *102*, 8364.
- (4) Elghanian, R.; Storhoff, J. J.; Mucic, R. C.; Letsinger, R. L.; Mirkin, C. A. *Science* **1997**, *277*, 1078.
- (5) Dirix, Y.; Bastiaansen, C.; Caseri, W.; Smith, P. *Adv. Mater.* **1999**, *11*, 223.
- (6) Ebbesen, T. W.; Lezec, H. J.; Ghaemi, H. F.; Thio, T.; Wolff, P. A. *Nature* **1998**, *391*, 667.
- (7) Knoll, W. *Annu. Rev. Phys. Chem.* **1998**, *49*, 569.
- (8) Quinten, M.; Leitner, A.; Krenn, J. R.; Aussenegg, F. R. *Opt. Lett.* **1998**, *23*, 1331.
- (9) Brongersma, M. L.; Hartman, J. W.; Atwater, H. A. *Phys. Rev. B* **2000**, *62*, R16356.
- (10) Egusa, S.; Liao, Y.-H.; Scherer, N. F. *Appl. Phys. Lett.* **2004**, *84*, 1257.
- (11) Freeman, R. G.; Grabar, K. C.; Allison, K. J.; Bright, R. M.; Davis, J. A.; Guthrie, A. P.; Hommer, M. B.; Jackson, M. A.; Smith, P. C.; Walter, D. G.; Natan, M. J. *Science* **1995**, *267*, 1629.
- (12) McFarland, A. D.; Young, M. A.; Dieringer, J. A.; Van Duyne, R. P. *J. Phys. Chem. B* **2005**, *109*, 11279.
- (13) Kahl, M.; Voges, E.; Kostrewa, S.; Viets, C.; Hill, W. *Sens. Actuators B* **1998**, *51*, 285.
- (14) Hulteen, J. C.; Van Duyne, R. P. *J. Vac. Sci. Technol. A* **1995**, *13*, 1553.
- (15) Haynes, C. L.; Van Duyne, R. P. *J. Phys. Chem. B* **2001**, *105*, 5599.
- (16) Wallraff, G. M.; Hinsberg, W. D. *Chem. Rev.* **1999**, *99*, 1801.
- (17) Ito, T.; Okazaki, S. *Nature* **2000**, *406*, 1027.
- (18) Haynes, C. L.; McFarland, A. D.; Zhao, L.; Van Duyne, R. P.; Schatz, G. C.; Gunnarsson, L.; Prikulis, J.; Kasemo, B.; Käll, M. *J. Phys. Chem. B* **2003**, *107*, 7337.
- (19) Craighead, H. G.; Niklasson, G. A. *Appl. Phys. Lett.* **1984**, *44*, 1134.
- (20) Piner, R. D.; Zhu, J.; Xu, F.; Hong, S.; Mirkin, C. A. *Science* **1999**, *283*, 661.
- (21) Canfield, B. K.; Kujala, S.; Jefimovs, K.; Vallius, T.; Turunen, J.; Kauranen, M. *J. Opt. A: Pure Appl. Opt.* **2005**, *7*, S110.
- (22) Bouhelier, A.; Bachelot, R.; Im, J. S.; Wiederrecht, G. P.; Lerondel, G.; Kostcheev, S.; Royer, P. *J. Phys. Chem. B* **2005**, *109*, 3195.
- (23) Félidj, N.; Aubard, J.; Lévi, G.; Krenn, J. R.; Schider, G.; Leitner, A.; Aussenegg, F. R. *Phys. Rev. B* **2002**, *66*, 245407.
- (24) Félidj, N.; Laurent, G.; Aubard, J.; Lévi, G.; Hohenau, A.; Krenn, J. R.; Aussenegg, F. R. *J. Phys. Chem. B* **2005**, *109*, 221103.
- (25) Hicks, E. M.; Zou, S.; Schatz, G. C.; Spears, K. G.; Van Duyne, R. P.; Gunnarsson, L.; Rindzevicius, T.; Kasemo, B.; Käll, M. *Nano Lett.* **2005**, *5*, 1065.
- (26) Lamprecht, B.; Schider, G.; Lechner, R. T.; Ditlbacher, H.; Krenn, J. R.; Leitner, A.; Aussenegg, F. R. *Phys. Rev. Lett.* **2000**, *84*, 4721.
- (27) Schider, G.; Krenn, J. R.; Gotschy, W.; Lamprecht, B.; Ditlbacher, H.; Leitner, A.; Aussenegg, F. R. *J. Appl. Phys.* **2001**, *90*, 3825.

- (28) Zhao, L.; Kelly, K. L.; Schatz, G. C. *J. Phys. Chem. B* **2003**, *107*, 7343.
- (29) Zou, S.; Janel, N.; Schatz, G. C. *J. Chem. Phys.* **2004**, *120*, 10871.
- (30) Zou, S.; Schatz, G. C. *J. Chem. Phys.* **2004**, *121*, 12606.
- (31) Carron, K. T.; Fluhr, W.; Meier, M.; Wokaun, A.; Lehmann, H. *W. J. Opt. Soc. Am. B* **1986**, *3*, 430.
- (32) Maier, S. A.; Brongersma, M. L.; Kik, P. G.; Atwater, H. A. *Phys. Rev. B* **2002**, *65*, 193408.
- (33) Malynych, S.; Chumanov, G. *J. Am. Chem. Soc.* **2003**, *125*, 2896.
- (34) Taleb, A.; Russier, V.; Courty, A.; Pileni, M. P. *Phys. Rev. B* **1999**, *59*, 13350.
- (35) Lamprecht, B.; Leitner, A.; Aussenegg, F. R. *Appl. Phys. B* **1999**, *68*, 419.
- (36) Moran, A. M.; Sung, J.; Hicks, E. M.; Van Duyne, R. P.; Spears, K. G. *J. Phys. Chem. B* **2005**, *109*, 4501.
- (37) Lamprecht, B.; Leitner, A.; Aussenegg, F. R. *Appl. Phys. B* **1997**, *64*, 269.
- (38) Canfield, B. K.; Kujala, S.; Jefimovs, K.; Turunen, J.; Kauranen, M. *Opt. Express* **2004**, *12*, 5418.
- (39) Tuovinen, H.; Kauranen, M.; Jefimovs, K.; Vahimaa, P.; Vallius, T.; Turunen, J.; Tkachenko, N. V.; Lemmetyinen, H. *J. Nonlinear Opt. Phys.* **2002**, *11*, 421.
- (40) Meier, M.; Wokaun, A.; Liao, P. F. *J. Opt. Soc. Am. B* **1985**, *2*, 931.
- (41) Zou, S.; Schatz, G. C. *J. Chem. Phys.* **2005**, *122*, 097102.
- (42) Mie, G. *Ann. Phys. (Leipzig)* **1908**, *25*, 377.
- (43) Kreibig, U.; Vollmer, M. *Optical Properties of Metal Clusters*; Springer-Verlag: Heidelberg, Germany, 1995; Vol. 25.
- (44) Kelly, K. L.; Coronado, E.; Zhao, L.; Schatz, G. C. *J. Phys. Chem. B* **2003**, *107*, 668.
- (45) Jensen, T. R.; Duval, M. L.; Kelly, K. L.; Lazarides, A. A.; Schatz, G. C.; Van Duyne, R. P. *J. Phys. Chem. B* **1999**, *103*, 9846.
- (46) Linden, S.; Christ, A.; Kuhl, J.; Giessen, H. *Appl. Phys. B* **2001**, *73*, 311.
- (47) Linden, S.; Kuhl, J.; Giessen, H. *Phys. Rev. Lett.* **2001**, *86*, 4688.
- (48) Canfield, B. K.; Kujala, S.; Kauranen, M.; Jefimovs, K.; Vallius, T.; Turunen, J. *Appl. Phys. Lett.* **2005**, *86*, 183109.